Title	Organic molecules in the protoplanetary disk of DG Tauri revealed by ALMA
Authors(s)	Podio, Linda, Bacciotti, Francesca, Fedele, D., Coffey, Deirdre
Publication date	2019-03-08
Publication information	Podio, Linda, Francesca Bacciotti, D. Fedele, and Deirdre Coffey. “Organic Molecules in the Protoplanetary Disk of DG Tauri Revealed by ALMA.” EDP Sciences, March 8, 2019. https://doi.org/10.1051/0004-6361/201834475.
Publisher	EDP Sciences
Item record/more information	http://hdl.handle.net/10197/11141
Publisher's version (DOI)	10.1051/0004-6361/201834475

A&A 623, L6 (2019)
https://doi.org/10.1051/0004-6361/201834475

Astronomy & Astrophysics

LETTER TO THE EDITOR

Organic molecules in the protoplanetary disk of DG Tauri revealed by ALMA

L. Podio[1], F. Bacciotti[1], D. Fedele[1], C. Favre[1], C. Codella[1,2], K. L. J. Rygl[3], I. Kamp[4], G. Guidi[5], E. Bianchi[2], C. Ceccarelli[2], D. Coffey[6,7], A. Garufi[1], and L. Testi[8,1]

[1] INAF – Osservatorio Astrofisico di Arcetri, Largo E. Fermi 5, 50125 Firenze, Italy
e-mail: `lpodio@arcetri.astro.it`
[2] Univ. Grenoble Alpes, IPAG, 38000 Grenoble, France
[3] INAF–Istituto di Radioastronomia & Italian ALMA Regional Centre, via P. Gobetti 101, 40129 Bologna, Italy
[4] Kapteyn Astronomical Institute, University of Groningen, Landleven 12, 9747 AD Groningen, The Netherlands
[5] ETH Zurich, Institute for Particle Physics and Astrophysics, Wolfgang-Pauli-Str. 27, 8093 Zurich, Switzerland
[6] School of Physics, University College Dublin, Belfield, Dublin 4, Ireland
[7] School of Cosmic Physics, The Dublin Institute for Advanced Studies, Dublin 2, Ireland
[8] European Southern Observatory (ESO), Karl-Schwarzschild-Str. 2, 85748 Garching, Germany

Received 19 October 2018 / Accepted 3 February 2019

ABSTRACT

Context. Planets form in protoplanetary disks and inherit their chemical compositions.

Aims. It is thus crucial to map the distribution and investigate the formation of simple organics, such as formaldehyde and methanol, in protoplanetary disks.

Methods. We analyze ALMA observations of the nearby disk-jet system around the T Tauri star DG Tau in the o − H_2CO $3_{1,2}-2_{1,1}$ and CH_3OH $3_{-2,2}-4_{-1,4}$ E, $5_{0,5}-4_{0,4}$ A transitions at an unprecedented resolution of ∼$0\overset{''}{.}15$, i.e., ∼18 au at a distance of 121 pc.

Results. The H_2CO emission originates from a rotating ring extending from ∼40 au with a peak at ∼62 au, i.e., at the edge of the 1.3 mm dust continuum. CH_3OH emission is not detected down to an rms of 3 mJy beam^{-1} in the 0.162 km s^{-1} channel. Assuming an ortho-to-para ratio of 1.8–2.8 the ring- and disk-height-averaged H_2CO column density is $\sim 0.3-4 \times 10^{14}$ cm^{-2}, while that of CH_3OH is $<0.04-0.7 \times 10^{14}$ cm^{-2}. In the inner 40 au no o − H_2CO emission is detected with an upper limit on its beam-averaged column density of $\sim 0.5-6 \times 10^{13}$ cm^{-2}.

Conclusions. The H_2CO ring in the disk of DG Tau is located beyond the CO iceline ($R_{\rm CO} \sim 30$ au). This suggests that the H_2CO abundance is enhanced in the outer disk due to formation on grain surfaces by the hydrogenation of CO ice. The emission peak at the edge of the mm dust continuum may be due to enhanced desorption of H_2CO in the gas phase caused by increased UV penetration and/or temperature inversion. The CH_3OH/H_2CO abundance ratio is <1, in agreement with disk chemistry models. The inner edge of the H_2CO ring coincides with the radius where the polarization of the dust continuum changes orientation, hinting at a tight link between the H_2CO chemistry and the dust properties in the outer disk and at the possible presence of substructures in the dust distribution.

Key words. protoplanetary disks – astrochemistry – ISM: molecules – stars: individual: DG Tau

1. Introduction

A key open question in astrochemistry is how chemical complexity increases during the formation process of Sun-like stars from prestellar cores to protoplanetary disks and ultimately to planets (Caselli & Ceccarelli 2012). Is the chemical composition of planets inherited from the prestellar and protostellar stages? Or does it reflect chemical processes occurring in the disk? Are organics efficiently formed in disks and by what mechanism(s)?

Organic and prebiotic molecules form either through gas-phase reactions (e.g., Millar et al. 1991; Balucani et al. 2015) or on the icy surface of dust grains (e.g., Tielens & Hagen 1982; Garrod et al. 2008). Understanding the efficiency and occurrence of these mechanisms requires a comparison of observations and predictions from astrochemical models. Detailed models of the disk chemistry including gas-phase reactions, molecule freeze-out, dust surface chemistry, and both thermal and non-thermal desorption mechanisms have been developed to predict the ice and gas abundances of complex organic molecules (e.g., Aikawa & Herbst 1999; Willacy & Woods 2009; Walsh et al. 2014; Loomis et al. 2015). However, only a few simple organics have been detected in disks so far (Qi et al. 2013; Öberg et al. 2015a; Walsh et al. 2016; Favre et al. 2018). Among these organics, formaldehyde (H_2CO) and methanol (CH_3OH) are essential to the investigation of the formation of organics. While H_2CO can form both in the gas phase and on grains, CH_3OH forms exclusively on grains (e.g., Watanabe & Kouchi 2002). Therefore, observations of its abundance and distribution in disks is crucial to constraining the mechanism(s) that form these simple organics, which are the building blocks in the formation of complex organic and prebiotic molecules.

Observationally, H_2CO has been detected in a number of protoplanetary disks through single-dish and low angular resolution surveys (e.g., Öberg et al. 2010, 2011; Guilloteau et al. 2013; Qi et al. 2013), but only three of them were imaged at an angular resolution of ∼0.5″, namely DM Tau (Loomis et al. 2015), TW Hya (Öberg et al. 2017), and HD 163296 (Carney et al. 2017). Therefore, the distribution and formation mechanisms (whether

Table 1. Properties of the observed lines.

Line	ν_0 (MHz)	E_{up} (K)	$S_{ij}\mu^2$ (D^2)	HPBW (PA)	rms (mJy beam^{-1})	F_{int} (mJy km s^{-1})	N_X (10^{14} cm^{-2})
o-H_2CO $3_{1,2}-2_{1,1}$	225 697.775	33	43.5	$0\farcs17\times0\farcs13$ (−20°)	1.7	292	0.2–2.7
CH_3OH $3_{-2,2}-4_{-1,4}$ E	230 027.060	40	0.7	$0\farcs16\times0\farcs13$ (−21°)	3	<1.6	<0.4–10
CH_3OH $5_{0,5}-4_{0,4}$ A	241 791.431	35	4	$0\farcs16\times0\farcs12$ (−21°)	3	<0.7	<0.04–0.7

in the gas phase or on grains) of H_2CO in disks is still unclear. Because of its low volatility and large partition function, CH_3OH is even more difficult to observe. To date, it has been detected only in the disks of TW Hya (Walsh et al. 2016) and of the young outbursting star V883 Ori (van 't Hoff et al. 2018).

The nearby T Tauri star DG Tau (d = 121 ± 2 pc; Gaia Collaboration 2016, 2018) is an ideal target to investigate the origin of simple organics in protoplanetary disks. DG Tau is surrounded by a compact and massive dusty disk imaged with CARMA (Isella et al. 2010) and ALMA in polarimetric mode (Bacciotti et al. 2018), and is associated with bright molecular emission detected with the IRAM 30 m telescope and *Herschel* (Guilloteau et al. 2013; Podio et al. 2012; Fedele et al. 2013). However, the origin of the detected molecular emission is unclear because DG Tau is also associated with a residual envelope and a jet (Eislöffel & Mundt 1998). Guilloteau et al. (2013) suggest that the single-peaked profile of SO and H_2CO is due to envelope emission, while the fundamental H_2O lines have double-peaked profiles and fluxes in agreement with disk model predictions (Podio et al. 2013). Interferometric maps of CO and its isotopologues show that the envelope dominate the molecular emission on large scales (Schuster et al. 1993; Kitamura et al. 1996), while disk emission is detected on scales <2″ (Testi et al. 2002; Güdel et al. 2018). Given the complexity of the circumstellar environment, spatially resolved maps are crucial to reveal the origin of the molecular emission.

In this letter we present ALMA Cycle 4 observations of H_2CO and CH_3OH in the disk of DG Tau at an unprecedented resolution of $\sim0\farcs15$, i.e., ∼18 au, and we discuss the possible formation mechanism of these simple organics.

2. Observations

ALMA observations of DG Tau were performed during Cycle 4 in August 2017 with baselines ranging from 17 m to 3.7 km. The bandpass was calibrated with the quasar J0510+1800, and phase calibration was performed every ∼8 min using quasar J0438+3004. The correlator setup consists of 12 high-resolution (0.122 MHz) spectral windows (SPWs) covering several molecular transitions, among which o-H_2CO $3_{1,2}-2_{1,1}$, and CH_3OH $3_{-2,2}-4_{-1,4}$ E and $5_{0,5}-4_{0,4}$ A (frequency, ν_0; upper level energies, E_{up}; and line strengths, $S_{ij}\mu^2$ are listed in Table 1). Data reduction was carried out following standard procedures using the ALMA pipeline in CASA 4.7.2. Self-calibration was performed on the source continuum emission, by combining a selection of line-free channels, and applying the phase solutions to the continuum-subtracted SPWs. Continuum images and spectral cubes were produced with tclean applying a manually selected mask and Briggs parameter of 0.5. The flux calibration was performed using quasars J0238+1636 and J0510+1800, obtaining an accuracy of ∼10%. The clean beam FWHMs and r.m.s (per 0.162 km s^{-1} channel) of the resulting line cubes are listed in Table 1. The continuum image has an rms of 0.3 mJy beam^{-1}.

3. Ring of formaldehyde in the disk of DG Tau

The map of the continuum emission at 225.7 GHz (1.3 mm) (Fig. 1) shows a smooth distribution, with integrated flux of 297 mJy and peak intensity of 33 mJy beam^{-1} at RA(J2000) = $04^h27^m04^s.70$, Dec(J2000) = +26°06′15″.72. By applying a 2D Gaussian fit, we determine the disk major and minor axes deconvolved from the beam ($0\farcs43\pm0\farcs02$ and $0\farcs38\pm0\farcs02$), hence the disk inclination i = 41° ± 2° and position angle PA = 128° ± 16°. These values are in good agreement with the estimates obtained at 0.87 mm and 1.3 mm (Bacciotti et al. 2018; Isella et al. 2010) and with the jet inclination and PA (the jet is ejected perpendicular to the disk at i_{jet} = 38° ± 2°, PA_{jet} = 226° ± 10°, Eislöffel & Mundt 1998).

The moment 0 and 1 maps of the H_2CO $3_{1,2}-2_{1,1}$ emission obtained with CASA by integrating over velocities from 3.24 to 9.24 km s^{-1}, and masking all pixels where no emission is detected above the 3σ level are shown in Fig. 1, while the moment 8 map obtained without applying a threshold is shown in Fig. A.2. Then radial intensity profiles of the H_2CO $3_{1,2}-2_{1,1}$ line and of the 1.3 mm continuum are obtained by azimuthally averaging the intensity maps after deprojecting for i = 41° and PA = 128° (see Fig. 2). The H_2CO $3_{1,2}-2_{1,1}$ moment maps show an H_2CO ring rotating around the central star which extends from ∼40 au to beyond the edge of the 1.3 mm dust emission ($R_{1.3\,mm}$ = 66 au at 3σ) (see also the channel maps in Fig. A.1). The intensity profile in Fig. 2 shows that the peak of the H_2CO emission is at ∼62 au (∼6.5 mJy beam^{-1} km s^{-1}). The 1D spectrum integrated over a $0\farcs33$–$0\farcs75$ ring area is centered at the systemic velocity V_{sys} = +6.24 km s^{-1} and shows a double-peaked profile (see Fig. A.3). Assuming Keplerian rotation around a 0.7 $M_\odot$ star as in Podio et al. (2013)[1] and i = 41°, the H_2CO peaks at $V_{LSR}-V_{sys}$ = ±1.95 km s^{-1} indicate an emitting radius of ∼70 au, in agreement with the position of the H_2CO ring.

The H_2CO line peak and integrated flux collected with the 11″ beam of the IRAM 30 m telescope (Guilloteau et al. 2013) is about a factor of four larger than that obtained integrating the ALMA cube over an 11″ circular area. This indicates that ALMA filters out the extended H_2CO emission from the outflow or the envelope, thus isolating the compact H_2CO emission from the disk.

4. Abundance of organic molecules

To estimate the H_2CO column density, the emission is integrated over a circular ring from $0\farcs33$ to $0\farcs75$ (40–90 au) and over the line velocity profile (between +3.24 and +9.24 km s^{-1}). The maps of the undetected CH_3OH lines are integrated over the same spatial region and velocity range as for the H_2CO line (i.e., the same pixels in RA, Dec, and V_{LSR}) to recover an upper

---

[1] The stellar mass obtained from the pre-main sequence tracks by Siess et al. (2000) is not affected by the change in distance (140 pc in previous studies) as the tracks are vertical in this region of the HR diagram.

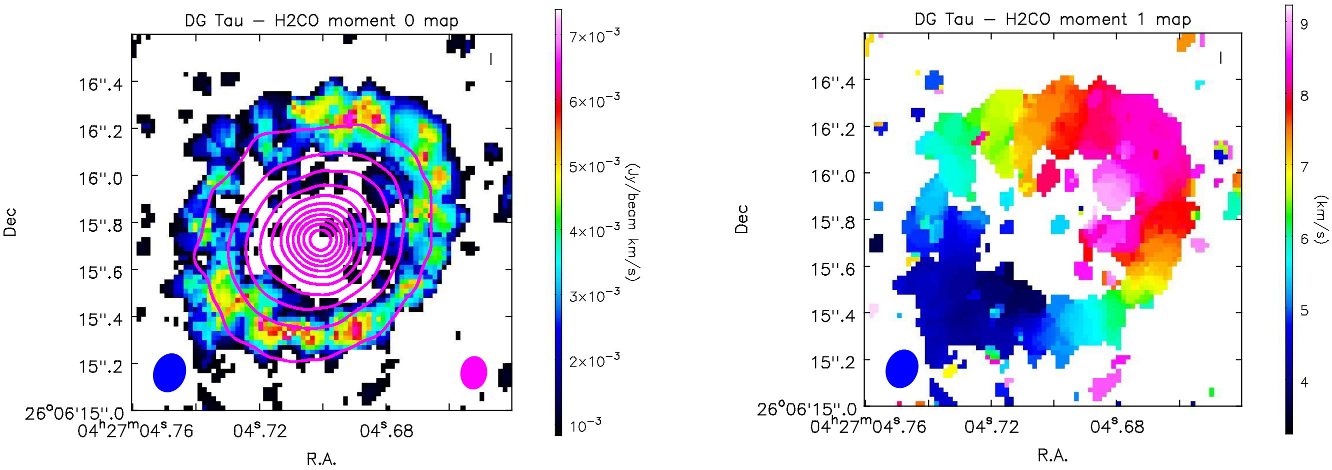

Fig. 1. Moment maps of H_2CO towards DG Tau. *Left panel*: H_2CO moment 0 map. The color scale indicates the line intensity integrated over the H_2CO velocity profile ($V_{\rm LSR}$ = (+3.24, +9.24) km s^{-1}) in Jy beam^{-1} km s^{-1}. The magenta contours indicate the 1.3 mm dust continuum emission (from 3σ with steps of 10σ). The blue and magenta ellipse in the bottom left and right corner indicate the synthesized beam for H_2CO and the continuum, respectively. *Right panel*: H_2CO moment 1 map. The color scale indicates the velocity $V_{\rm LSR}$ in km s^{-1}.

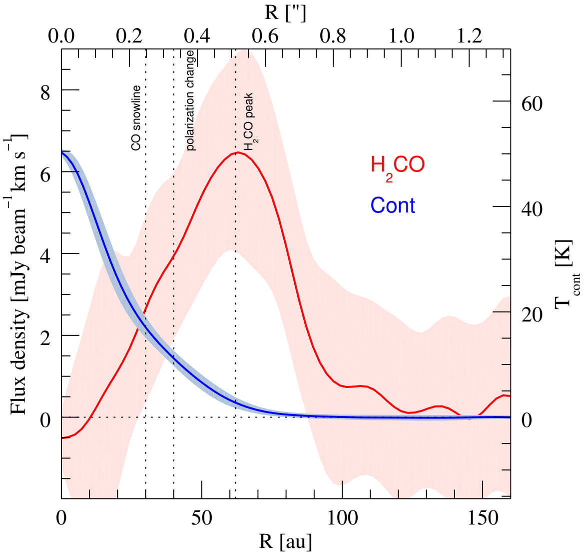

Fig. 2. Azimuthally averaged radial intensity profile of H_2CO $3_{1,2}-2_{1,1}$ (in mJy beam^{-1} km s^{-1}, red line) and of the 1.3 mm continuum (in K, blue line). For the continuum the conversion factor from brightness temperature to flux density is 0.65 mJy beam^{-1} K^{-1}. The shaded areas indicate the dispersion of the intensity values around the mean along each annulus in the radial direction. The vertical black dotted lines indicate the position of the CO iceline, the change in the polarization orientation, and the H_2CO emission peak.

limit on the methanol column density under the assumption that CH_3OH originates from the same disk region as H_2CO. The ring-averaged o-H_2CO and CH_3OH column densities, $N_{\rm o-H_2CO}$ and $N_{\rm CH_3OH}$, are derived from the integrated line intensities by assuming local thermodynamic equilibrium (LTE) and optically thin emission (see, e.g., Eqs. (1) and (2) in Bianchi et al. 2017), and adopting the molecular parameters and partition function from the Cologne Database of Molecular Spectroscopy (CDMS, Müller et al. 2001). The assumption of LTE is clearly justified as the gas density near the midplane and in the intermediate disk layers where H_2CO is thought to originate (see, e.g, Walsh et al. 2014; Öberg et al. 2017, and the discussion in Sect. 5) is high (from $\sim 10^8$ to $\sim 10^{12}$ cm^{-3} according to the disk model by Podio et al. 2013), i.e., well above the critical density of the H_2CO $3_{1,2}-2_{1,1}$ transition ($n_{\rm cr} \sim 7-4.6\times10^5$ cm^{-3} at 20−100 K, Shirley 2015). The gas temperature in these intermediate disk layers is between 30 and 300 K according to the same disk model. Therefore, assuming an excitation temperature $T_{\rm ex}$ = 30−300 K we infer an average o-H_2CO column density over the ring and the disk height of ~0.2–2.7 × 10^{14} cm^{-2}. Following the same procedure as for H_2CO, the most stringent constraint on the CH_3OH column density is derived from the CH_3OH 241.791 GHz line (which has the greatest line strength $S_{ij}\mu^2 \sim 4$ D^2): $N_{\rm CH_3OH} < 0.04$–0.7×10^{14} cm^{-2}. The inferred column densities are summarized in Table 1. The total H_2CO column density is then obtained by assuming an ortho-to-para ratio of 1.8–2.8 (Guzmán et al. 2018): $N_{\rm H_2CO} \sim 0.3-4\times10^{14}$ cm^{-2}. Using the H_2 column density in the outer disk (>40 au) from the disk model by Podio et al. (2013) ($N_{\rm H} \sim 0.3-1\times10^{25}$ cm^{-2}), we estimate the ring- and disk-height-averaged abundance of organic molecules: $X_{\rm H_2CO} \sim 6\times10^{-12}-3\times10^{-10}$, $X_{\rm CH_3OH} < 0.8\times10^{-12}-5\times10^{-11}$. Finally, in the inner 40 au no o-H_2CO is detected above 3σ. Taking into account the wider velocity range over which the emission may be spread, this provides an upper limit on the o-H_2CO beam-averaged column density of ~0.5–6 × 10^{13} cm^{-2}.

The inferred H_2CO column density and abundance, and the upper limits retrieved for CH_3OH are in agreement with the predictions of chemistry models of protoplanetary disks around T Tauri stars (see, e.g., Walsh et al. 2014). These models predict gas-phase fractional abundances in the disk outer regions (r > 50 au) of between 10^{-13} and a few 10^{-10} for H_2CO and CH_3OH. The H_2CO abundance is in agreement within a factor of a few with that estimated in the disk of TW Hya and HD 163296 assuming $T_{\rm ex}$ = 25 K (Carney et al. 2019), while it is up to two orders of magnitude lower than that found in disks with large inner holes, for example Oph IRS48 and AB Aur where the outer disk reservoir of icy organics is directly exposed to stellar illumination (van der Marel et al. 2014; Pacheco-Vázquez et al. 2016). Also, the nondetection of the targeted methanol transitions is consistent with a CH_3OH/H_2CO ratio <1, in agreement with the prediction of chemical models (e.g., Walsh et al. 2014) and with the upper limit found in the disk of HD 163296 (CH_3OH/H_2CO < 0.24), while it is lower than that estimated in the disk of TW Hya (CH_3OH/H_2CO = 1.27) (Carney et al. 2019).

5. H_2CO formation

Disk chemistry models by Willacy & Woods (2009), Walsh et al. (2014) and Loomis et al. (2015) show that H_2CO can form either in the gas phase, primarily through the reaction CH_3 + O; or on dust grains via hydrogenation of CO locked in their icy mantles (CO + H –> HCO + H -> H_2CO). The gas-phase CH_3 + O formation route is efficient in the warm inner region and upper layers of the disk where atomic oxygen is produced by photodissociation of gas-phase CO. On the contrary, formation on grains occurs in the cold outer disk beyond the CO iceline where CO is condensed onto grains and available for H_2CO formation.

Resolved observations of H_2CO emission allow us to constrain the formation mechanism of H_2CO in disks. The H_2CO radial intensity profile in the disk of DG Tau (Fig. 2) shows characteristics in common with the three other disks observed at high angular resolution with ALMA (DM Tau, Loomis et al. 2015; TW Hya, Öberg et al. 2017; and HD 163296, Carney et al. 2017): (i) the depression (or lack) of emission in the inner disk; (ii) the emission peak located outside the CO iceline; (iii) emission beyond the mm dust continuum (with a peak at the edge of the continuum in the case of DG Tau, TW Hya, and HD 163296).

In the case of the HD 163296 disk, it was argued that the central depression of the H_2CO emission is caused by absorption by optically thick dust continuum (Carney et al. 2017), while Öberg et al. (2017) explain it as a real drop in abundance in TW Hya. For DG Tau, we can exclude problems due to continuum subtraction as the line-free channels of the continuum subtracted cube do not show negative flux values in the central regions. To evaluate if absorption by the dust continuum affects the observed H_2CO intensity, we estimate the optical depth of the disk at 1.3 mm from the dust opacity and surface density given by Isella et al. (2010). According to their modeling, the disk is optically thick in the innermost region ($\tau_{1.3\,\mathrm{mm}} > 1$ at <3 au or <9 au, depending on whether the self-similarity or power-law parametrization for the surface density is adopted). Then the optical depth rapidly drops to ~0.5 at 20 au and <0.3 for $r >$ 30 au[2]. On the other hand, observations of ^{13}CO 2-1 and $C^{18}O$ 2-1 show a hole in the inner 25 au, which could be due to the thickness of the continuum up to this radius (Güdel et al. 2018). To further check the continuum optical depth we compared its brightness temperature (T_{cont}, see Fig. 2) to the expected dust temperature T_{dust} by Podio et al. (2013) (their Fig. 2, where $T_{\mathrm{gas}} = T_{\mathrm{dust}}$ in the midplane). We found $T_{\mathrm{cont}}/T_{\mathrm{dust}} < 0.6$, hence $\tau < 1$, for $r > 25$ au, which indicates that the continuum should be optically thin beyond this radius, in agreement with the observed distribution of ^{13}CO 2-1 and $C^{18}O$ 2-1. Finally, we checked the H_2CO $3_{1,2} - 2_{1,1}$ line opacity by using the non-LTE radiative transfer code RADEX (van der Tak et al. 2007). Assuming column densities up to $N_{\mathrm{H_2CO}} \sim 10^{15}\,\mathrm{cm^{-2}}$ in the inner disk region (10 – 40 au) (Walsh et al. 2014), a line width of ~6 km $\mathrm{s^{-1}}$, and gas densities and temperatures from our ProDiMo DG Tau model ($n_{\mathrm{H_2}} \sim 10^{10}$–$10^{12}\,\mathrm{cm^{-3}}$ and $T_{\mathrm{gas}} >$ 30 K at 10–40 au and intermediate disk height), the H_2CO line optical depth reach a maximum value of ~1. Therefore, we conclude that the H_2CO ring is related to an increase in the H_2CO abundance beyond ~40 au.

As shown by Loomis et al. (2015), disk models that include only H_2CO gas-phase formation produce centrally peaked column density and emission profiles, and strongly underestimate the observed H_2CO emission in the outer disk. H_2CO formation on grains followed by desorption in the gas phase has to be taken into account to increase the H_2CO column densities and line emission in the outer disk (by up to two orders of magnitude in the case of DM Tau). The intensity profile of H_2CO in the disk of DG Tau shows a steep increase in the outer disk with an emission peak at 62 au. Interestingly, the thermo-chemical ProDiMo disk model presented in Podio et al. (2013), which matches the long wavelength part of the SED of DG Tau and the *Herschel*/HIFI water lines, shows that the CO iceline, R_{CO}, is located at ~30 au[3]. The fact that the peak is located outside the CO iceline suggests that the outer H_2CO reservoir is mainly produced by CO hydrogenation on grains. This is in agreement with disk chemistry models and with observations by Loomis et al. (2015), Öberg et al. (2017) and Carney et al. (2017). Contrary to the disks of DM Tau, TW Hya, and HD 163296, in the case of DG Tau no H_2CO emission is detected in the inner disk, where gas-phase formation dominates. As discussed above, this could be due to absorption by the optically thick dust continuum (up to ~25 au) and to a lower H_2CO abundance (by a factor of ≤10) and column density in the inner 40 au (see Sect. 4). Also taking into account the wider velocity range over which the emission may be spread, this would produce no detectable emission in the present observations (rms ~1.7 mJy $\mathrm{beam^{-1}}$). Finally, the fact that the H_2CO emission peaks at the edge of the mm dust continuum and extends beyond it could be due to a steeper decrease in the density of the gas and of the small grains at this location. As small grains are responsible for the opacity at UV wavelengths, the UV radiation penetrates deeper in the disk and more efficiently photodesorbs H_2CO from grains (Öberg et al. 2015b, 2017). Moreover, Cleeves (2016) suggests that there could be a temperature inversion at the edge of the large dust population, which would enhance thermal desorption. Alternatively, H_2CO could be efficiently formed in the gas phase beyond the mm-dust edge due to more efficient photodissociation of CO favoring the CH_3 + O formation route (Carney et al. 2017). An enhancement of molecular emission at the edge of the millimeter dust continuum has been observed in a number of disks (Öberg et al. 2015b, 2017; Huang et al. 2016; Carney et al. 2017, 2018), but a test of the proposed mechanisms would require higher angular resolution observations of multiple molecules and detailed modeling.

6. Disk chemistry and dust properties

The H_2CO $3_{1,2} - 2_{1,1}$ ring is asymmetric as the redshifted side is ~1.5 times brighter than the blueshifted side (Figs. 1, A.2, and A.3). The same asymmetry is observed in the map of the linearly polarized intensity of the continuum at 0.87 mm by Bacciotti et al. (2018), where the redshifted disk side is brighter than the blueshifted side in the outer 40–50 au region. The map by Bacciotti et al. (2018) also indicates that the orientation of the linear polarization vector changes from parallel to the disk minor axis in the inner disk region to azimuthal in the outer 40–50 au. Interestingly, the radius where the change in the orientation of polarization occurs is coincident with the inner radius of the H_2CO ring. The intensity and orientation of the polarization of the dust continuum caused by self-scattering strongly depends on the dust size, opacity, and degree of settling (Yang et al. 2017). This suggests that the H_2CO chemistry

---

[2] At the adopted distance of 121 pc the radius where the disk becomes optically thin is ~15% smaller with respect to the modeling by Isella et al. (2010) who adopted $d = 140$ pc.

[3] R_{CO} is derived from a steady-state solution of a chemical network including gas-phase chemistry as well as adsorption and (non)thermal desorption processes (e.g., Kamp et al. 2010) for a stellar luminosity $L_* \sim 1\,L_\odot$ at 140 pc. At the adopted distance of 121 pc, L_* decreases by ~25%, hence the estimated R_{CO} is an upper limit.

is closely connected to the dust properties in the outer disk. For example, a drop in the dust opacity beyond 40 au could be responsible for the change in polarization (Bacciotti et al. 2018). If the opacity of small grains also decreases, this would cause an enhancement of H_2CO desorbed from grains, due to increased UV and X-ray penetration. In the case of DG Tau, the desorption mechanism could be also favored by UV and X-rays produced in the blueshifted jet shocks (Coffey et al. 2007; Güdel et al. 2008) that directly illuminate the disk from above. The chemical and polarization change at 40 au could also be linked to the existence of substructures in the dust distribution. The radial profile of the continuum intensity along the projected disk major axis shows a shoulder of emission at about 40 au (see Fig. B.1), which supports this hypothesis.

Finally, it is interesting to note that the H_2CO ring is offset by $\sim 0''.06$ ($\sim$7 au) with respect to the dust continuum peak, i.e., the redshifted ring side is located farther from the continuum peak than the blueshifted side (Fig. 1). This also suggests an asymmetric distribution of the chemically enriched gas in the outer disk region. However, higher angular resolution observations are needed to confirm this scenario.

7. Conclusions

ALMA observations at $0''.15$ resolution of the disk of DG Tau show a ring of formaldehyde peaking at $\sim$62 au, i.e., outside the CO iceline ($R_{\rm CO} \sim 30$ au) and close to the edge of the 1.3 mm dust continuum ($R_{\rm dust} \sim 66$ au). This suggests an enhancement of the H_2CO abundance in the outer disk due to H_2CO formation by CO hydrogenation on the icy grains. Moreover, the desorption of H_2CO from the grains could be enhanced at the edge of the mm dust continuum due to increased UV penetration and/or temperature inversion. The abundance ratio between CH_3OH and H_2CO is <1, in agreement with the predictions of disk chemistry models. Interestingly, the inner edge of the H_2CO ring is at $\sim$40 au, where the polarization of the dust continuum changes orientation and the continuum intensity shows a local enhancement, hinting at a tight link between the H_2CO chemistry and the dust properties in the outer disk and at the possible presence of substructures in the dust distribution.

Acknowledgements. This paper uses ALMA data from project 2016.1.00846.S. ALMA is a partnership of ESO (representing its member states), NSF (USA), and NINS (Japan), together with NRC (Canada), MOST and ASIAA (Taiwan), and KASI (Republic of Korea), in cooperation with the Republic of Chile. The Joint ALMA Observatory is operated by ESO, AUI/NRAO, and NAOJ. This work was partly supported by PRIN-INAF/2016 GENESIS-SKA and by the Italian Ministero dell'Istruzione, Università e Ricerca through the grants Progetti Premiali 2012/iALMA (CUP-C52I13000140001), 2017/FRONTIERA (CUP-C61I15000000001), and SIR-(RBSI14ZRHR). GG acknowledges the financial support of the Swiss National Science Foundation within the framework of the National Centre for Competence in Research PlanetS.

References

Aikawa, Y., & Herbst, E. 1999, A&A, 351, 233
Bacciotti, F., Girart, J. M., Padovani, M., et al. 2018, ApJ, 865, L12
Balucani, N., Ceccarelli, C., & Taquet, V. 2015, MNRAS, 449, L16
Bianchi, E., Codella, C., Ceccarelli, C., et al. 2017, MNRAS, 467, 3011
Carney, M. T., Hogerheijde, M. R., Loomis, R. A., et al. 2017, A&A, 605, A21
Carney, M. T., Fedele, D., Hogerheijde, M. R., et al. 2018, A&A, 614, A106
Carney, M. T., Hogerheijde, M. R., Guzmán, V. V., et al. 2019, A&A, in press, DOI: 10.1051/0004-6361/201834353
Caselli, P., & Ceccarelli, C. 2012, A&ARv, 20, 56
Cleeves, L. I. 2016, ApJ, 816, L21
Coffey, D., Bacciotti, F., Ray, T. P., Eislöffel, J., & Woitas, J. 2007, ApJ, 663, 350
Eislöffel, J., & Mundt, R. 1998, AJ, 115, 1554
Favre, C., Fedele, D., Semenov, D., et al. 2018, ApJ, 862, L2
Fedele, D., Bruderer, S., van Dishoeck, E. F., et al. 2013, A&A, 559, A77
Gaia Collaboration (Prusti, T., et al.) 2016, A&A, 595, A1
Gaia Collaboration (Brown, A. G. A., et al.) 2018, A&A, 616, A1
Garrod, R. T., Widicus Weaver, S. L., & Herbst, E. 2008, ApJ, 682, 283
Güdel, M., Skinner, S. L., Audard, M., Briggs, K. R., & Cabrit, S. 2008, A&A, 478, 797
Güdel, M., Eibensteiner, C., Dionatos, O., et al. 2018, A&A, 620, L1
Guilloteau, S., Di Folco, E., Dutrey, A., et al. 2013, A&A, 549, A92
Guzmán, V. V., Öberg, K. I., Carpenter, J., et al. 2018, ApJ, 864, 170
Huang, J., Öberg, K. I., & Andrews, S. M. 2016, ApJ, 823, L18
Isella, A., Natta, A., Wilner, D., Carpenter, J. M., & Testi, L. 2010, ApJ, 725, 1735
Kamp, I., Tilling, I., Woitke, P., Thi, W.-F., & Hogerheijde, M. 2010, A&A, 510, A18
Kitamura, Y., Kawabe, R., & Saito, M. 1996, ApJ, 457, 277
Loomis, R. A., Cleeves, L. I., Öberg, K. I., Guzman, V. V., & Andrews, S. M. 2015, ApJ, 809, L25
Millar, T. J., Herbst, E., & Charnley, S. B. 1991, ApJ, 369, 147
Müller, H. S. P., Thorwirth, S., Roth, D. A., & Winnewisser, G. 2001, A&A, 370, L49
Öberg, K. I., Qi, C., Fogel, J. K. J., et al. 2010, ApJ, 720, 480
Öberg, K. I., Qi, C., Fogel, J. K. J., et al. 2011, ApJ, 734, 98
Öberg, K. I., Guzmán, V. V., Furuya, K., et al. 2015a, Nature, 520, 198
Öberg, K. I., Furuya, K., Loomis, R., et al. 2015b, ApJ, 810, 112
Öberg, K. I., Guzmán, V. V., Merchantz, C. J., et al. 2017, ApJ, 839, 43
Pacheco-Vázquez, S., Fuente, A., Baruteau, C., et al. 2016, A&A, 589, A60
Podio, L., Kamp, I., Flower, D., et al. 2012, A&A, 545, A44
Podio, L., Kamp, I., Codella, C., et al. 2013, ApJ, 766, L5
Qi, C., Öberg, K. I., & Wilner, D. J. 2013, ApJ, 765, 34
Schuster, K. F., Harris, A. I., Anderson, N., & Russell, A. P. G. 1993, ApJ, 412, L67
Shirley, Y. L. 2015, PASP, 127, 299
Siess, L., Dufour, E., & Forestini, M. 2000, A&A, 358, 593
Testi, L., Bacciotti, F., Sargent, A. I., Ray, T. P., & Eislöffel, J. 2002, A&A, 394, L31
Tielens, A. G. G. M., & Hagen, W. 1982, A&A, 114, 245
van der Marel, N., van Dishoeck, E. F., Bruderer, S., & van Kempen, T. A. 2014, A&A, 563, A113
van der Tak, F. F. S., Black, J. H., Schöier, F. L., Jansen, D. J., & van Dishoeck, E. F. 2007, A&A, 468, 627
van 't Hoff, M. L. R., Tobin, J. J., Trapman, L., et al. 2018, ApJ, 864, L23
Walsh, C., Millar, T. J., Nomura, H., et al. 2014, A&A, 563, A33
Walsh, C., Loomis, R. A., Öberg, K. I., et al. 2016, ApJ, 823, L10
Watanabe, N., & Kouchi, A. 2002, ApJ, 571, L173
Willacy, K., & Woods, P. M. 2009, ApJ, 703, 479
Yang, H., Li, Z.-Y., Looney, L. W., Girart, J. M., & Stephens, I. W. 2017, MNRAS, 472, 373

Appendix A: H_2CO channel maps, moment 8 map, and 1D spectrum

The channel maps and the moment 8 map obtained from the H_2CO $3_{12}-2_{11}$ line cube towards DG Tau are shown in Figs. A.1 and A.2. The moment 8 map strongly supports the ring detection with a $S/N \sim 5$.

The 1D spectrum obtained integrating the H_2CO line cube over a circular ring extending from 0.″33 to 0.″75 is shown in Fig. A.3.

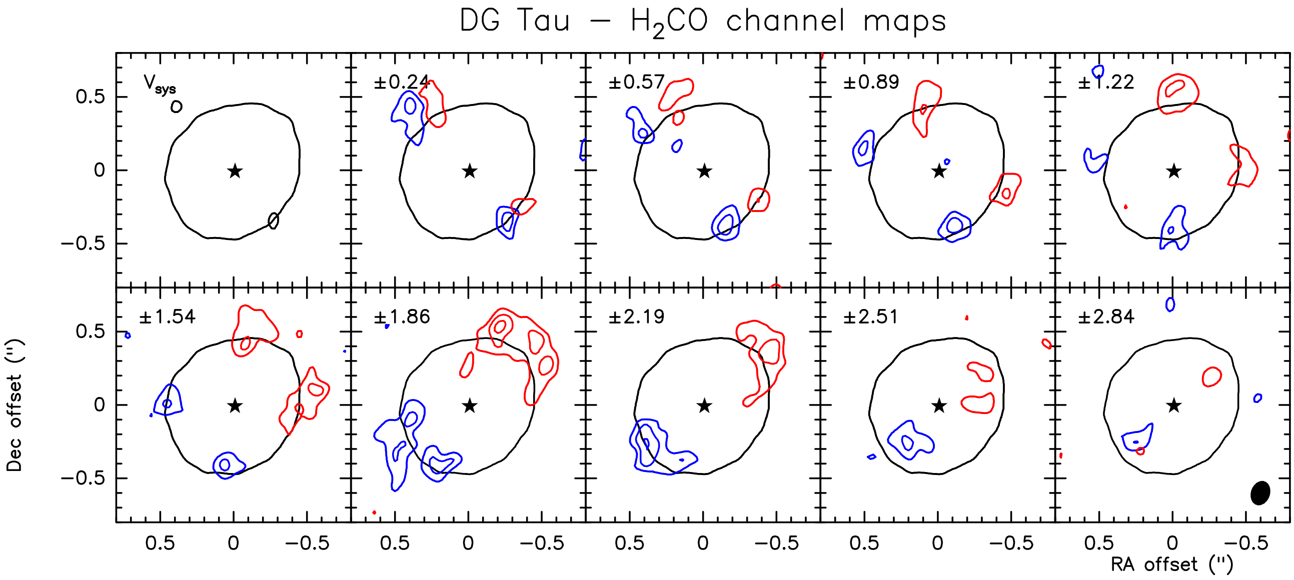

Fig. A.1. Channel maps of H_2CO $3_{12}-2_{11}$ towards DG Tau. The blue and red contours show the emission at symmetric blue- and redshifted velocities with respect to systemic (V_{sys} = +6.24 km s^{-1}), as labeled in the upper right corner ($V - V_{sys}$ in km s^{-1}). The first contour is at 5σ with steps of 3σ. The black star and contour indicates the peak and the 5σ level of the 1.3 mm continuum. The ellipse in the bottom right corner of the last channel map shows the ALMA synthesized beam.

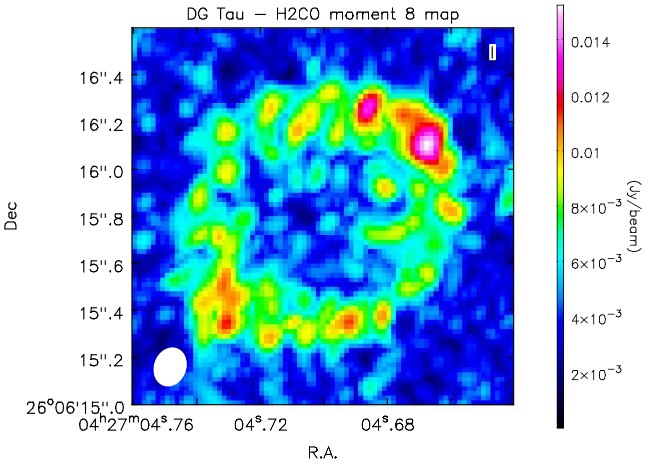

Fig. A.2. H_2CO moment 8 map towards DG Tau. The color scale indicates the line intensity in Jy beam^{-1}. The white ellipse in the bottom left corner indicates the synthesized beam.

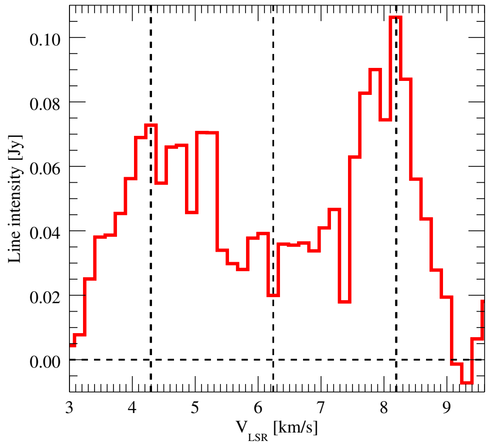

Fig. A.3. H_2CO $3_{1,2}-2_{1,1}$ spectrum integrated over a 0.″33–0.″75 ring area. The vertical dashed lines indicate the systemic velocity, V_{sys} = +6.24 km s^{-1}, and the position of the blue- and redshifted peaks ($V_{peak} = V_{sys} \pm 1.95$ km s^{-1}).

Appendix B: Analysis of the continuum radial intensity profile

In Fig. B.1 we plot the radial profile of the continuum intensity along the projected disk major axis, in order to achieve the highest resolution, and avoid the dilution of possible substructures in the dust flux that could result from azimuthal averaging. No strong asymmetries are visible between the northwest and the southeast sides of the disk. A tentative shoulder appears at about 40 au from the star: to characterize its position we computed the second derivative of the radial intensity profile (by calculating the differentials over bins of 5 au, averaged between the NW and SE sides). The radii at which the second derivative becomes negative give us the locations where there is a local increase in the continuum intensity and the profile becomes locally convex. This occurs in the central region (<11.5 au), corresponding to the peak of the continuum, and in the range between 38 and 44.5 au where the small shoulder is visible in the intensity profile. Hence, the center of the observed continuum intensity enhancement is located at ~41 au.

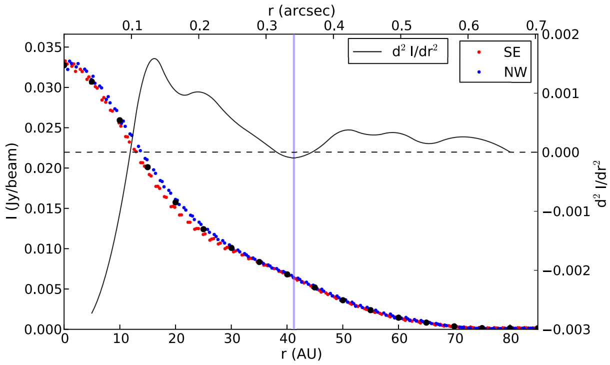

Fig. B.1. Radial cut of the continuum intensity map of DG Tau at 1.3 mm: every point corresponds to a pixel inside a half-beam across the disk major axis (i = 41°, PA = 128°). Red dots represent the southeast side of the disk, blue dots the northwest side. The large black dots correspond to 5 au bins computed by averaging the two sides. The black curve is the second derivative of the continuum intensity profile. The solid vertical line indicates the center of the continuum enhancement, at 41 au.